

## Supporting Information

### Table of content:

#### S1. Anode preparation

#### S2. Examination of different carbon-based substrates

S2.1 Carbon nanotube (CNT) mats

S2.2 Activated carbon cloth

S2.3 Hydrophilic carbon cloth

S2.4 Plain carbon cloth

#### S3. Additional material characterizations

S3.1 X-ray diffraction

S3.2 FIB sample preparation

S3.3 Qualitative EDS analysis

S3.4 HRSEM micrographs

#### S4. Quantitative chemical composition analysis

S4.1. Inductively coupled plasma atomic emission spectroscopy (ICP-AES)

S4.2 Energy dispersive X-ray spectroscopy (EDS) and wavelength dispersive X-ray spectroscopy (WDS)

#### S5. Electrochemical characterizations

#### S6. E-TAC tests

#### S7. Dissolved oxygen measurements

## S1. Anode preparation

The anodes were prepared by electrochemical deposition of cobalt-doped nickel hydroxide onto carbon cloth (CC, plain carbon cloth, 1071 HCB, Fuel cell store, 99.5% carbon content) or nickel foam (NF, Ni-4753, RECEMAT, 95.2% porosity with 400  $\mu\text{m}$  average pore size) substrates. Digital images of the CC- and NF-supported anodes are presented in Figures S1a and S1b, respectively. Figure S2 shows a digital image of a rolled CC substrate. Figures S3a and S3b show a digital image and an illustration, respectively, of the deposition setup we used.

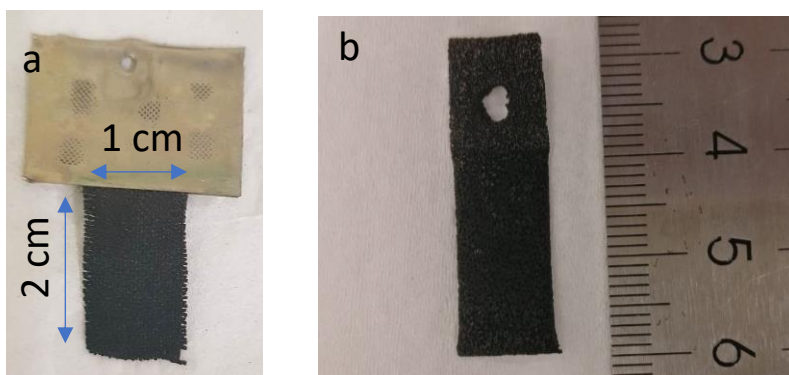


Figure S1: Photograph of electrochemically deposited nickel hydroxide anodes supported on carbon cloth (a) and nickel foam (b) substrates.



Figure S2: Photograph of a rolled carbon cloth substrate .

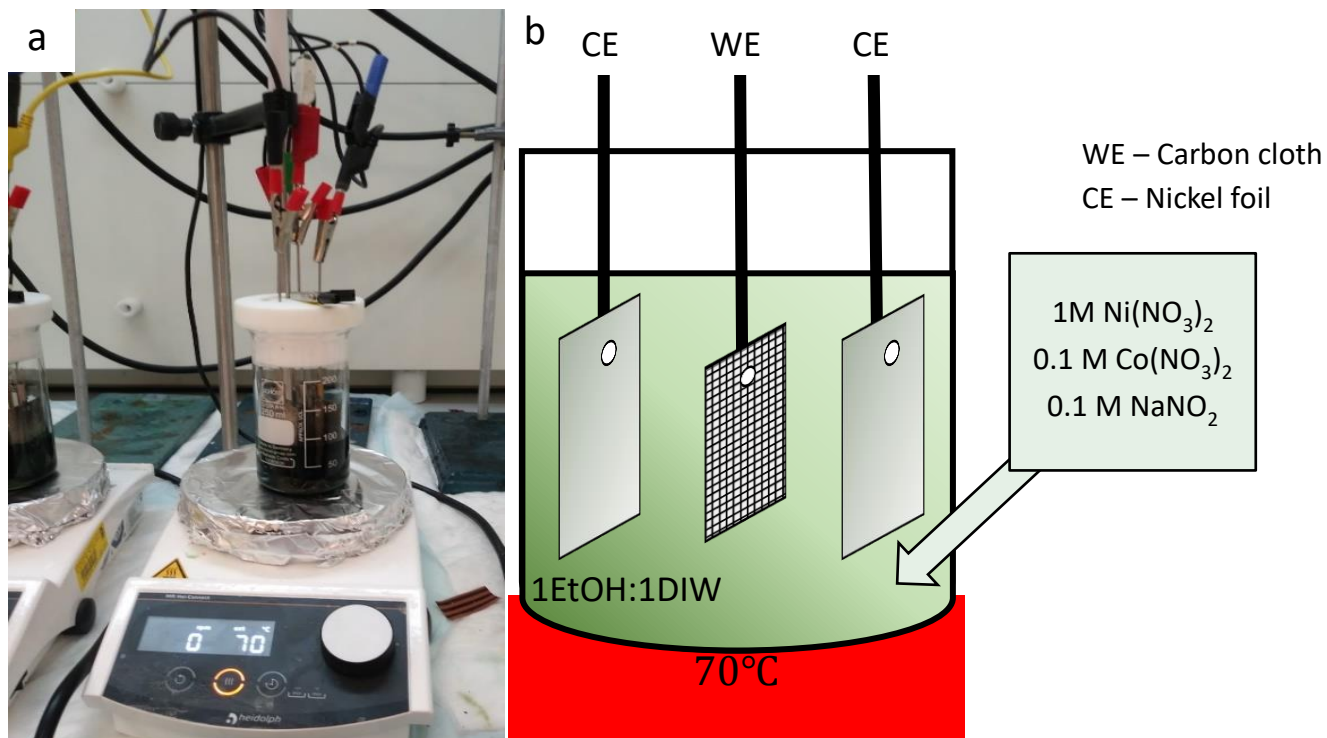


Figure S3: Photograph (a) and schematic illustration (b) of the setup used for electrochemical deposition. The setup comprised of a closed beaker partially filled with the deposition solution, and three electrodes: one working electrode (WE) and two counter electrodes (CE), dipped in the solution. The beaker was placed on a hot plate and kept at a constant temperature of 70°C, and the electrodes were connected to a potentiostat.

## S2. Examination of different carbon-based substrates

### S2.1. Carbon nanotube (CNT) mats

Non-woven carbon nanotube (CNT) mats (10, 20 and 50  $\mu\text{m}$  thick mats, C-255-H2B by Tortech Nano Fibers) were initially examined as potential substrates for the electrochemically deposited anodes. Tortech's CNT mats are made of non-woven ultra-long CNTs. They are flexible, easy to handle, with high electrical conductivity and stability in alkaline electrolytes.

Nickel hydroxide was electrochemically deposited onto the CNT mats following a similar recipe to that described in the article. Figure S4 presents SEM micrographs of samples deposited at a constant current of 30  $\text{mA}/\text{cm}^2$  for different times. The deposition yielded a uniform coating on top of the CNT mat instead of conformal coating of the CNTs as we hoped, even at short deposition times (10 min, Figure S6c-d). This coating morphology does not utilize the high surface area of the CNTs. Therefore, we decided not to continue with these substrates.

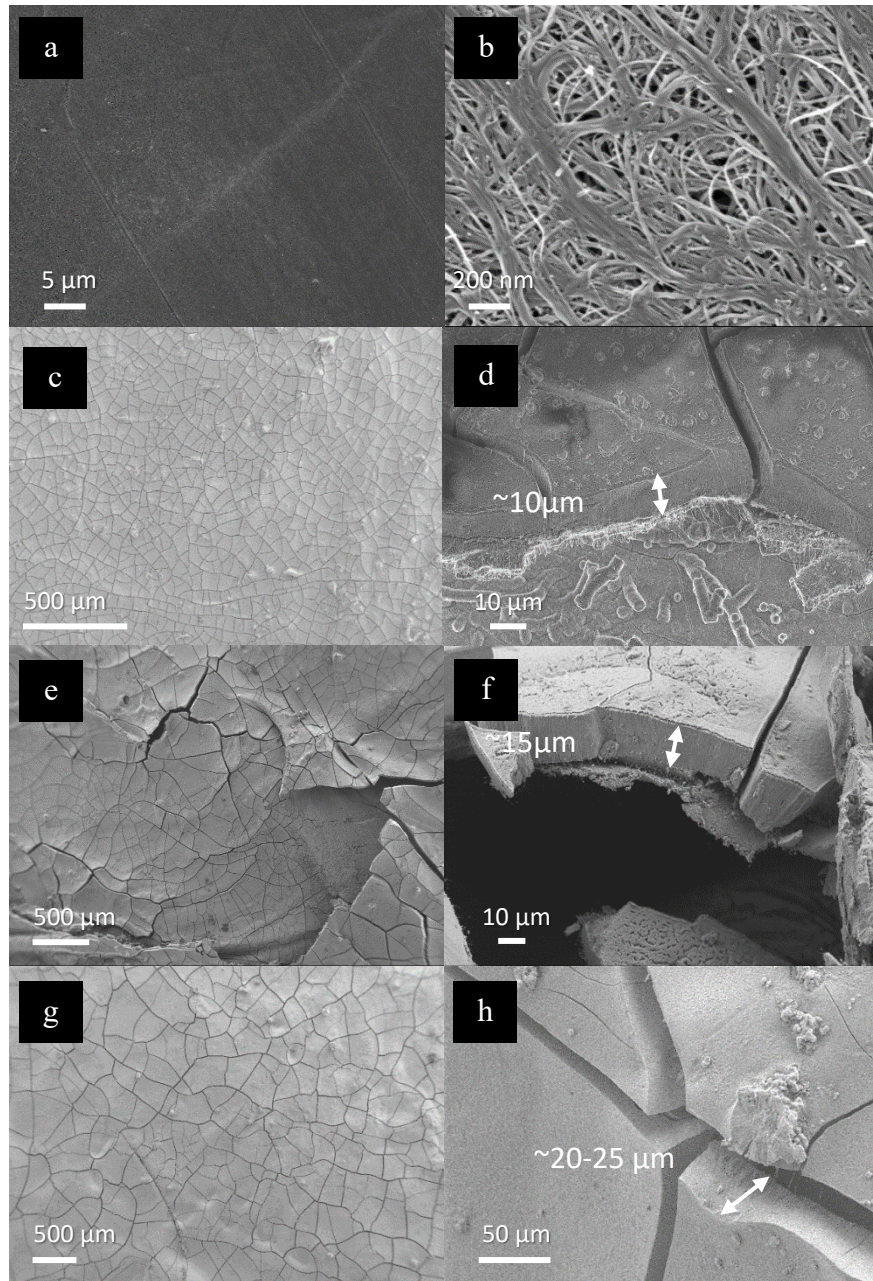


Figure S4: SEM micrographs of a bare CNT mat (a)-(b), and nickel hydroxide layers deposited onto CNT mats at 30 mA/cm<sup>2</sup> for 10 (c)-(d), 40 (e)-(f) and 60 min (g)-(h).

## S2.2. Activated carbon cloth

Activated carbon fibers (ACF) have attracted attention for their very high specific surface area ( $>2500 \text{ m}^2/\text{g}$ ), large pore volume ( $>0.8 \text{ cm}^3/\text{g}$ ), and narrow micropore size distribution. Oxidation treatments (*e.g.*, using oxygen or hydrogen peroxide) of the ACFs are employed to develop high-specific surface area. Figure S5 presents HRSEM images of a bare activated carbon cloth (ACC 5092-15 by Kynol).

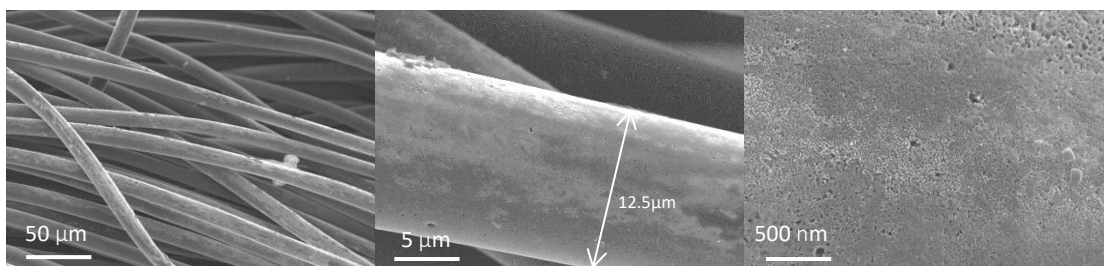


Figure S5: HRSEM micrographs of a bare activated carbon cloth (ACC-5092-15) at different magnifications.

As can be seen in Figure S5 the ACC fibers have a diameter of  $\sim 12.5 \mu\text{m}$ , with small micro-craters on the surface, which are probably formed by the activation process. The electrical resistance of this substrate was too high, as can be seen by the four-point probe (4PP) I-V curves presented in Figure S6. The ACC displays a non-Ohmic behavior. The calculated resistivity from the linear regions marked in orange and grey is  $5.66 \Omega\cdot\text{cm}$ , which is too high for high-efficiency anodes. Thus, operating at a current density of  $10 \text{ mA}/\text{cm}^2$  would yield an internal resistance (*IR*) loss of  $57 \text{ mV}$  per  $\text{cm}$ , too high for practical application.

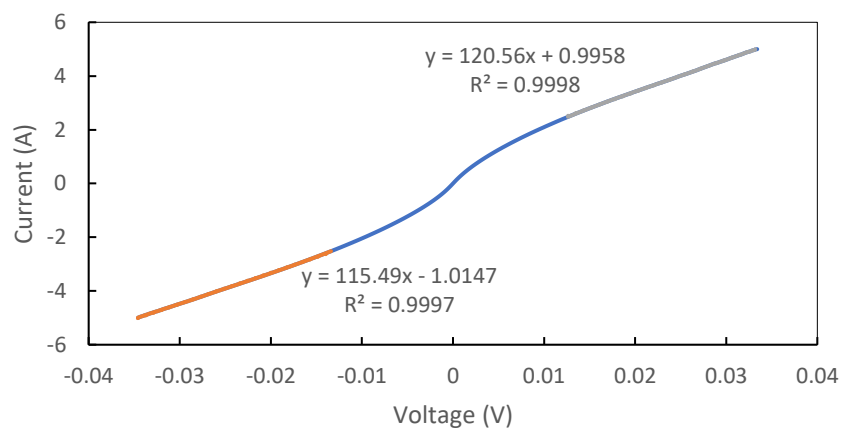


Figure S6: 4PP I-V curve of a bare activated carbon cloth (ACC-5092-15).

### S2.3. Hydrophilic carbon cloth

A thin hydrophilic carbon cloth (ELAT® - Hydrophilic Plain Cloth, ETC Fuel cell, 406  $\mu\text{m}$ ) made of woven 10  $\mu\text{m}$  carbon fibers was examined. The hydrophilic carbon cloth (HCC) has 80% porosity and an areal density of 0.013  $\text{g}/\text{cm}^2$  according to the manufacturer. Figure S7 presents HRSEM images of the bare HCC.

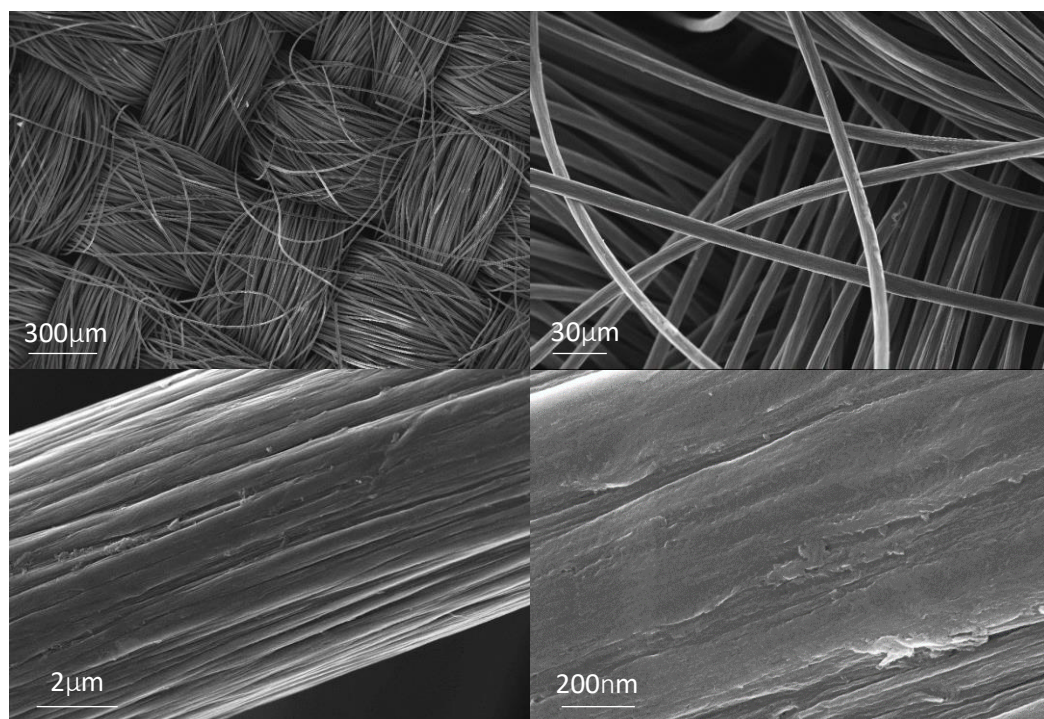


Figure S7: HRSEM micrographs of a bare hydrophilic carbon cloth.

As shown in Figure S7, the diameter of the HCC fibers is about 10  $\mu\text{m}$ , and their surface display longitudinal etching trenches along the fibers, probably due to their activation process. The 4PP I-V curve of this substrate is presented in Figure S8.

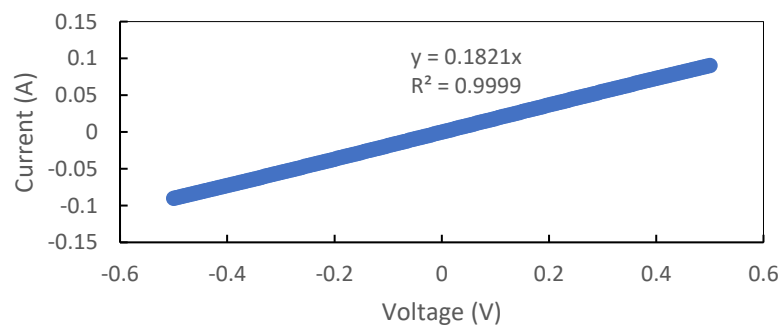


Figure S8: Probe station analysis results for a hydrophilic carbon cloth.

As shown in Figure S8, the linear I-V relation indicate an Ohmic behavior. The calculated resistivity is  $170 \text{ m}\Omega \cdot \text{cm}$ , an order of magnitude lower than that of the ACC. This substrate passed the initial selection criteria, and was further examined through electrochemical deposition following the same recipe as described in the article.

Figure S9 presents HRSEM micrographs of nickel hydroxide anodes deposited on HCC substrates at a current density of  $30 \text{ mA/cm}^2$  for 10, 30 and 60 min. Conformal coating around the fibers is shown for all the layers, in contrast to the outer layer deposition on the CNT mat in Figure S6. However, the adhesion to the fibers was not strong, and many segments of the layer were peeled off the fibers, indicating weak adhesion between the deposited nickel hydroxide layer and the hydrophilic carbon cloth. After 10 min deposition, the deposited layer is mostly uniform, and it has a thickness of about  $0.2 \text{ }\mu\text{m}$ . After 30 min deposition, there are more peeled off segments, but the deposition layer is still mostly intact, with a larger thickness of about  $3 \text{ }\mu\text{m}$ . After 1 h deposition, most of the layer was peeled off the fibers, and its thickness is approximately  $10 \text{ }\mu\text{m}$ . Although the ACC substrate displays suitable macro structure and electrical conductivity, it was deemed as unsuitable for our application due to the weak adhesion of the deposited nickel hydroxide layer to the hydrophilic ACC substrate. These results suggested that plain carbon cloth without the activation pretreatment that turns the substrate hydrophilic might be suitable. Therefore, the next substrate that was examined is plain carbon cloth, produced by the same manufacturer as the hydrophilic carbon cloth, but without the activation surface pretreatment.

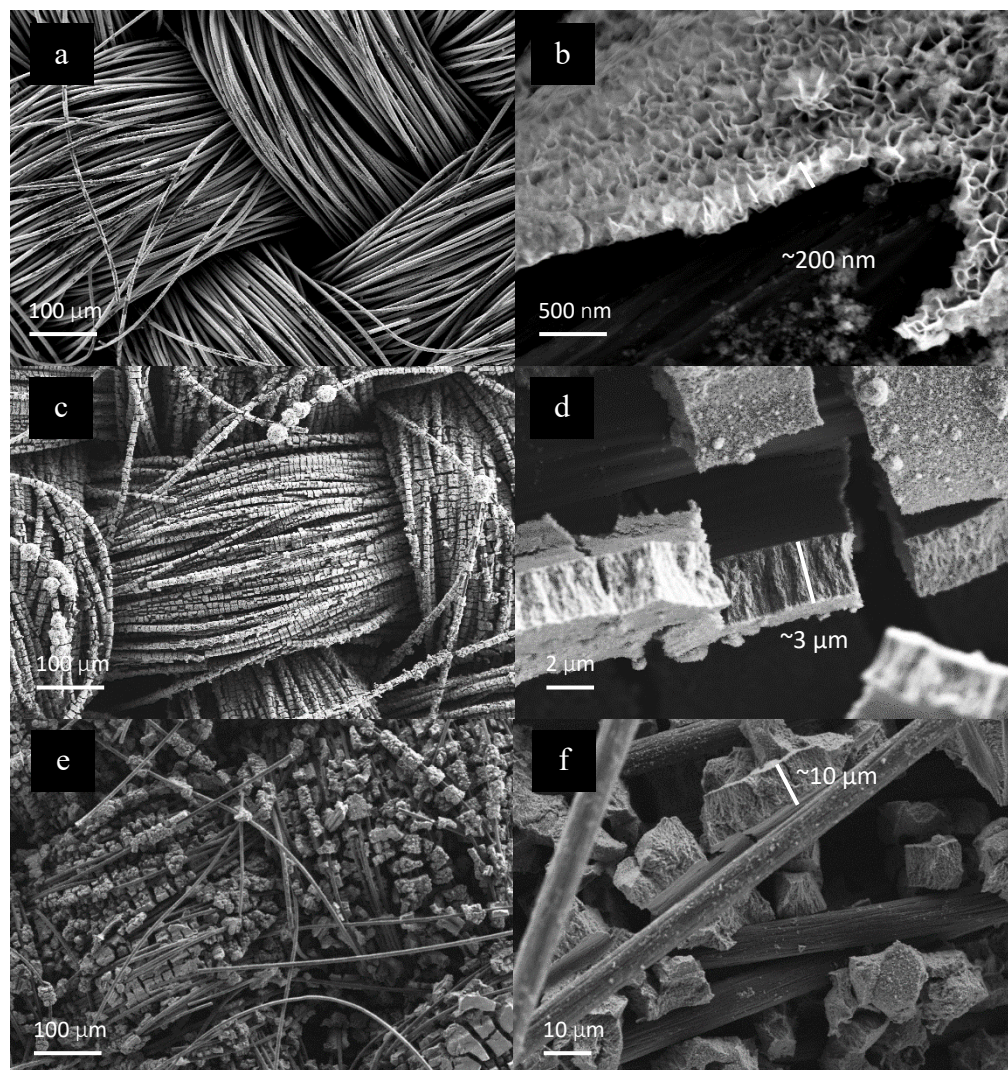


Figure S9: HRSEM micrographs of nickel hydroxide anodes deposited on hydrophilic carbon cloth substrates at a current density of 30 mA/cm<sup>2</sup> for 10 (a-b), 30 (c-d), and 60 min (e-f).

#### S2.4. Plain carbon cloth

Plain carbon cloth (PCC, ETC Fuel cell) is a thin (356 μm) and flexible substrate. The PCC is made of woven carbon fibers with a diameter of 7.5 μm. It has a density of 1.75 -1.77 g/cm<sup>3</sup>, surface area of 0.62 g/cm<sup>3</sup> and electrical resistivity of  $1.1 \cdot 10^{-3} \Omega \cdot \text{cm}$  according to the manufacturer. PCC does not undergo any activation treatment at the manufacturing process. Thus, it has a lower porosity and a higher density compared to the HCC and ACC substrates that we examined before. Although higher porosity contributes to the surface area, the micro-porosity may not contribute to the electrochemical performance of anodes with a thick layer of nickel hydroxide deposited onto the substrate. For example, deposition on the ultra-

long CNT non-woven mats showed that a pore size of 10-100 nm is not beneficial to the electrodeposited nickel hydroxide since its thickness is much larger than this pore size

Figure S10 presents HRSEM image of the PCC, and Figure shows its 4PP I-V curve.

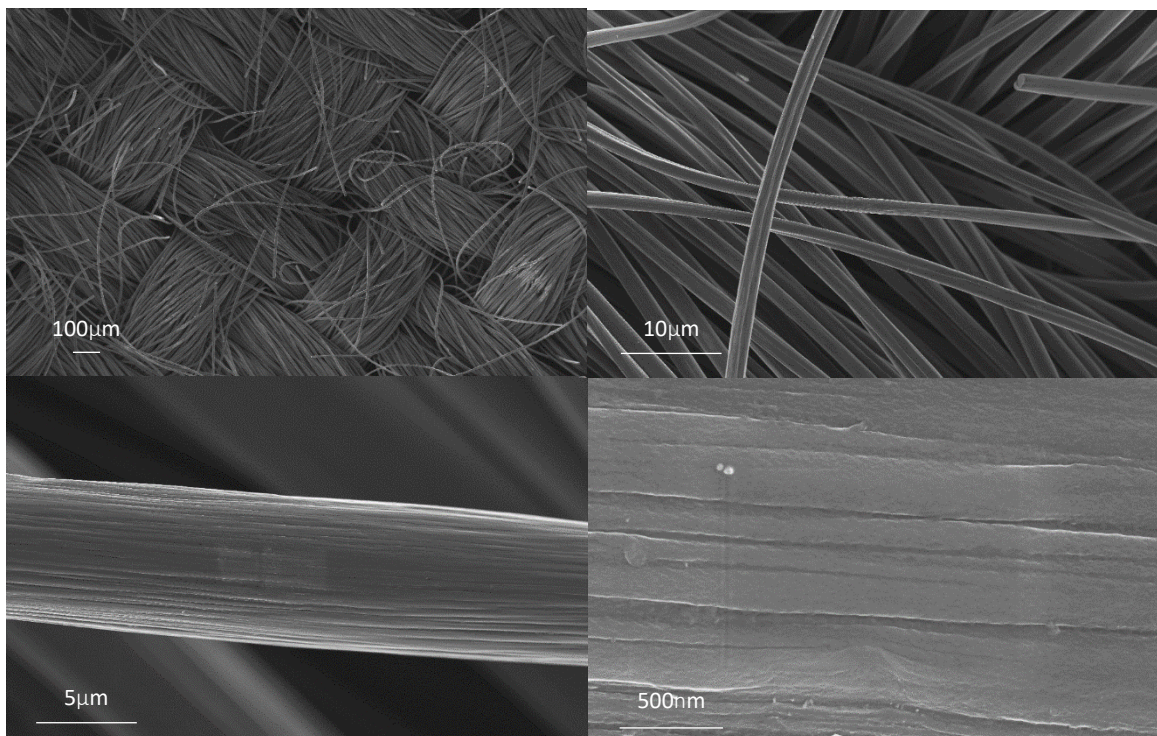


Figure S10: HRSEM micrographs of a bare plain carbon cloth (PCC 1071).

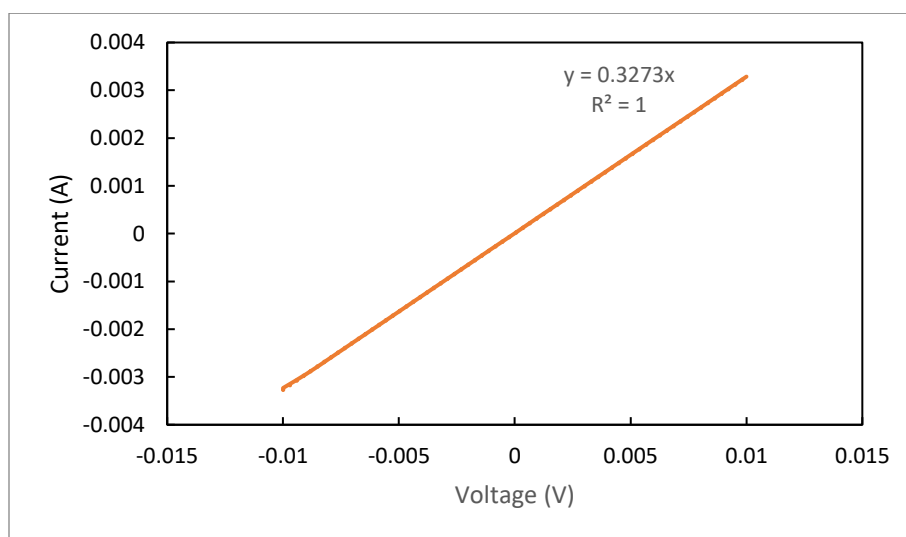


Figure S11: 4PP I-V curve of a bare plain carbon cloth.

As shown in Figure S11, the linear relation between the voltage and the current displays Ohmic behavior with specific resistivity of  $16 \text{ m}\Omega \cdot \text{cm}$ , an order of magnitude lower than that of the HCC. PCC was selected as the most promising substrate for the rest of this study due to its suitable macroscopic structure and surface morphology and low resistivity. In addition, strong adhesion has been achieved between this substrate and the nickel hydroxide layer as shown in the article.

## S3. Additional material characterizations

### S3.1. X-ray diffraction

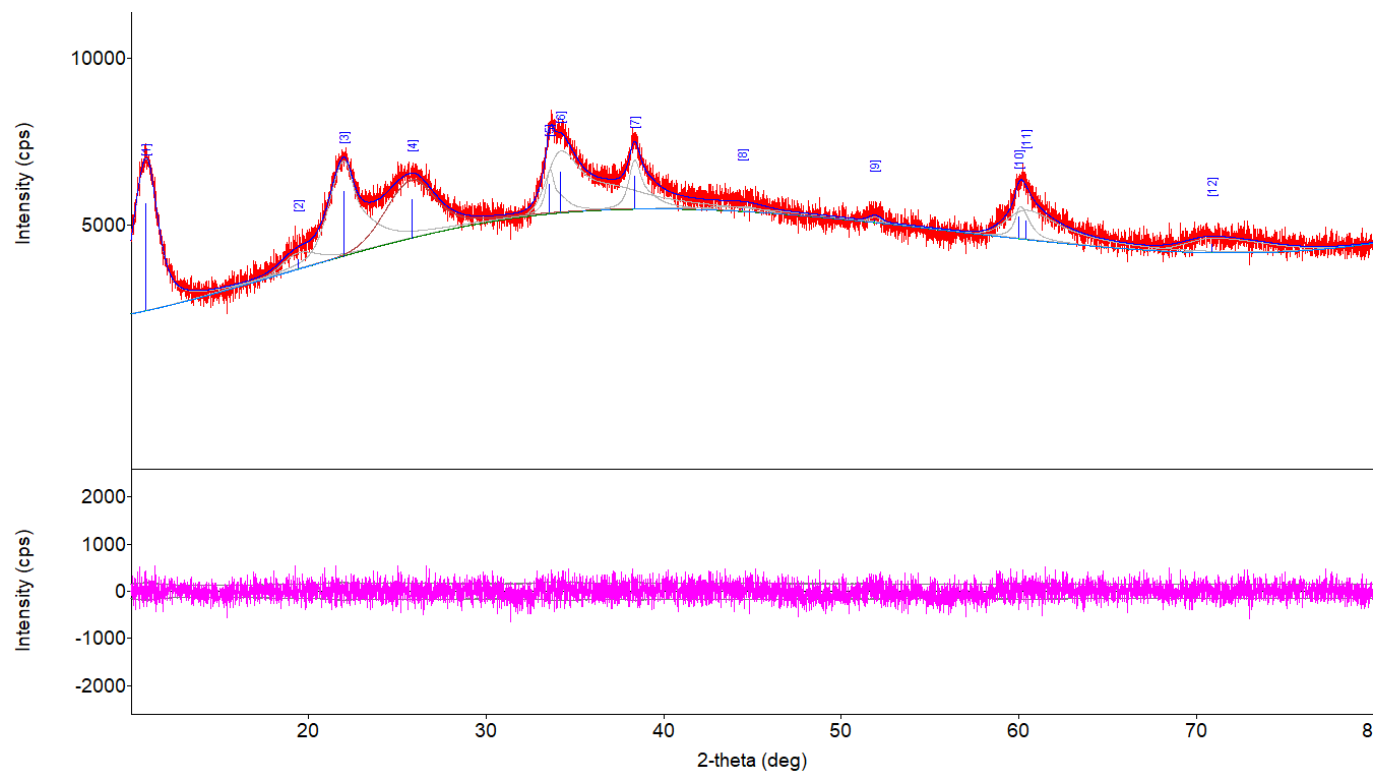


Figure S12. Fitting of the XRD pattern of the as-synthesized cobalt-doped  $\text{Ni}(\text{OH})_2$  anode. Fitting was done by means of the PDXL2 (version 2.8.1.1) using pseudo-Voigt peak profile. In the top image: Red noisy curve is the measured signal; light blue is a manually fitted background curve; light green is fitting. The peaks are numbers 1 through 12 and ascribed in Table S1. In the bottom image: residual signal (fitted signal extracted from the measure one).

Table S1. Phase identification for the as-synthesized cobalt-doped Ni(OH)<sub>2</sub> anode. Peak numbers (#) correspond to Figure S12. ICDD 00-038-0715 and 00-014-0117 were used as references for the  $\alpha$ -Ni(OH)<sub>2</sub> and  $\beta$ -Ni(OH)<sub>2</sub> phases, respectively. d (Å) – d-spacing; FWHM (deg) – full width at half maximum; Int. I (cps deg) – peak intensity; Size (Å) – domain size.

#	2 $\theta$ (deg)	Expected 2 $\theta$ (deg) (from the relevant crystallographic database)	Phase/Plane	d (Å)	FWHM (deg)	Int. I (cps deg)	Size (Å)
1	10.9	11.349	(003) $\alpha$ -Ni(OH) <sub>2</sub>	8.1471	1.5	4776	56
2	19.4	19.258	(001) $\beta$ -Ni(OH) <sub>2</sub>	4.5652	2.4	720	36
3	22.0	22.725	(006) $\alpha$ -Ni(OH) <sub>2</sub>	4.0427	1.8	4469	48
4	25.8	N/A	Amorphous halo of carbon	3.4467	3.1	3849	27
5	33.6	33.458	(101) $\alpha$ -Ni(OH) <sub>2</sub>	2.6672	0.6	978	136
6	34.2	34.412	(012) $\alpha$ -Ni(OH) <sub>2</sub>	2.6207	2.6	5296	33
7	38.3	38.765	(015) $\alpha$ -Ni(OH) <sub>2</sub>	2.3462	0.9	1364	98
8	44.4	45.985	(018) $\alpha$ -Ni(OH) <sub>2</sub>	2.0379	3.3	407	27
9	51.9	52.1	(102) $\beta$ -Ni(OH) <sub>2</sub>	1.7608	0.8	84	113
10	60.0	59.981	(110) $\alpha$ -Ni(OH) <sub>2</sub>	1.5405	0.9	750	109
11	60.4	61.254	(113) $\alpha$ -Ni(OH) <sub>2</sub>	1.5311	3.6	2501	27
12	70.9	N/A	?	1.3284	5.3	1348	19

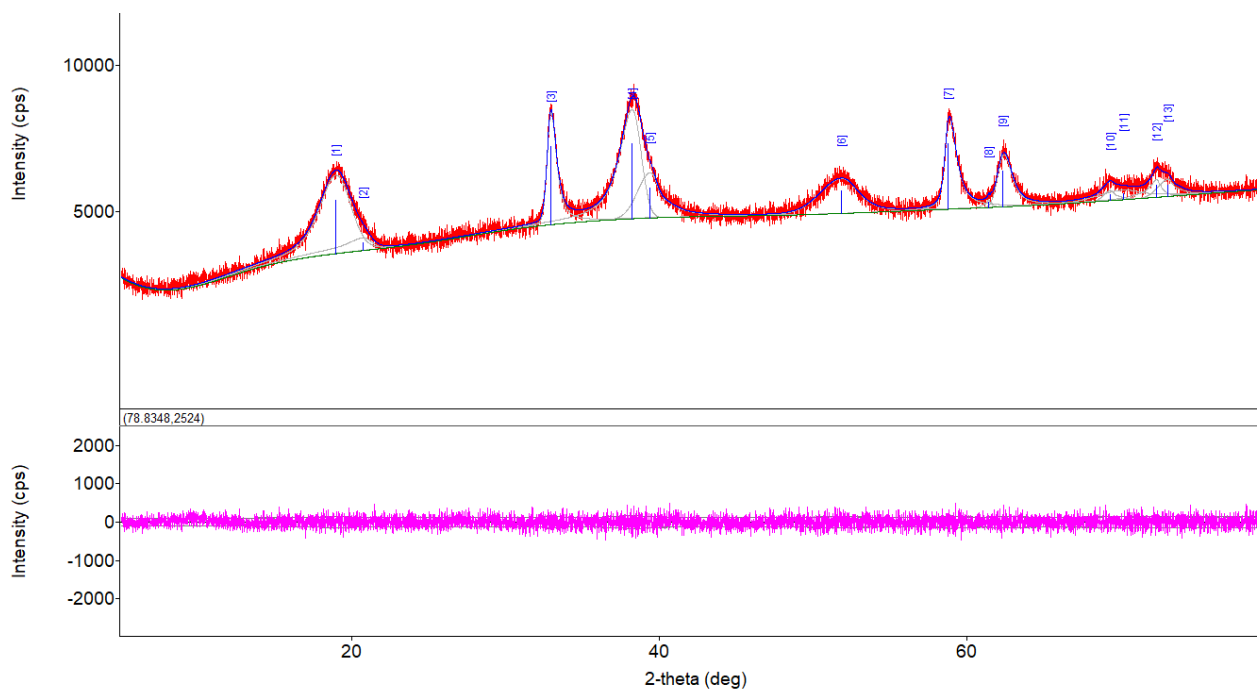


Figure S13. Fitting of the XRD pattern of the chemically aged cobalt-doped Ni(OH)<sub>2</sub> anode. Fitting was done by means of the PDXL2 (version 2.8.1.1) using pseudo-Voigt peak profile. In the top image: Red noisy curve is the measured signal; light blue is a manually fitted background curve; light green is fitting. The peaks are numbers 1 through 13 and ascribed in Table S2. In the bottom image: residual signal (fitted signal extracted from the measure one).

Table S2. Phase identification for the chemically aged cobalt-doped Ni(OH)<sub>2</sub> anode. Peak numbers (#) correspond to Figure S13. ICDD 00-014-0117 file used as references for the β-Ni(OH)<sub>2</sub> phase. d (Å) – d-spacing; FWHM (deg) – full width at half maximum; Int. I (cps deg) – peak intensity; Size (Å) – domain size.

#	2θ (deg)	Expected 2θ (deg) (from the relevant crystallographic database)	Phase/Plane	d (Å)	FWHM (deg)	Int. I (cps deg)	Size (Å)
1	18.9	19.258	(001) β-Ni(OH) <sub>2</sub>	4.6804	2.3	4311	36
2	20.7	N/A	?	4.2845	2.2	832	38
3	32.9	33.064	(100) β-Ni(OH) <sub>2</sub>	2.7187	0.7	2191	129
4	38.2	38.541	(101) β-Ni(OH) <sub>2</sub>	2.3546	1.6	4873	56
5	39.4	39.098	(002) β-Ni(OH) <sub>2</sub>	2.2853	1.7	2090	53
6	51.8	52.100	(102) β-Ni(OH) <sub>2</sub>	1.7629	2.9	2489	32
7	58.8	59.052	(110) β-Ni(OH) <sub>2</sub>	1.5703	0.8	2471	117
8	61.4	60.240	(003) β-Ni(OH) <sub>2</sub>	1.5087	0.2	96	388
9	62.3	62.726	(111) β-Ni(OH) <sub>2</sub>	1.4885	1.1	1502	92
10	69.3	69.346	(200) β-Ni(OH) <sub>2</sub>	1.3549	0.8	237	127
11	70.1	70.478	(103) β-Ni(OH) <sub>2</sub>	1.3408	3.4	902	30
12	72.3	72.737	(201) β-Ni(OH) <sub>2</sub>	1.3053	0.8	565	126
13	73.0	73.130	(112) β-Ni(OH) <sub>2</sub>	1.2943	1.1	581	90

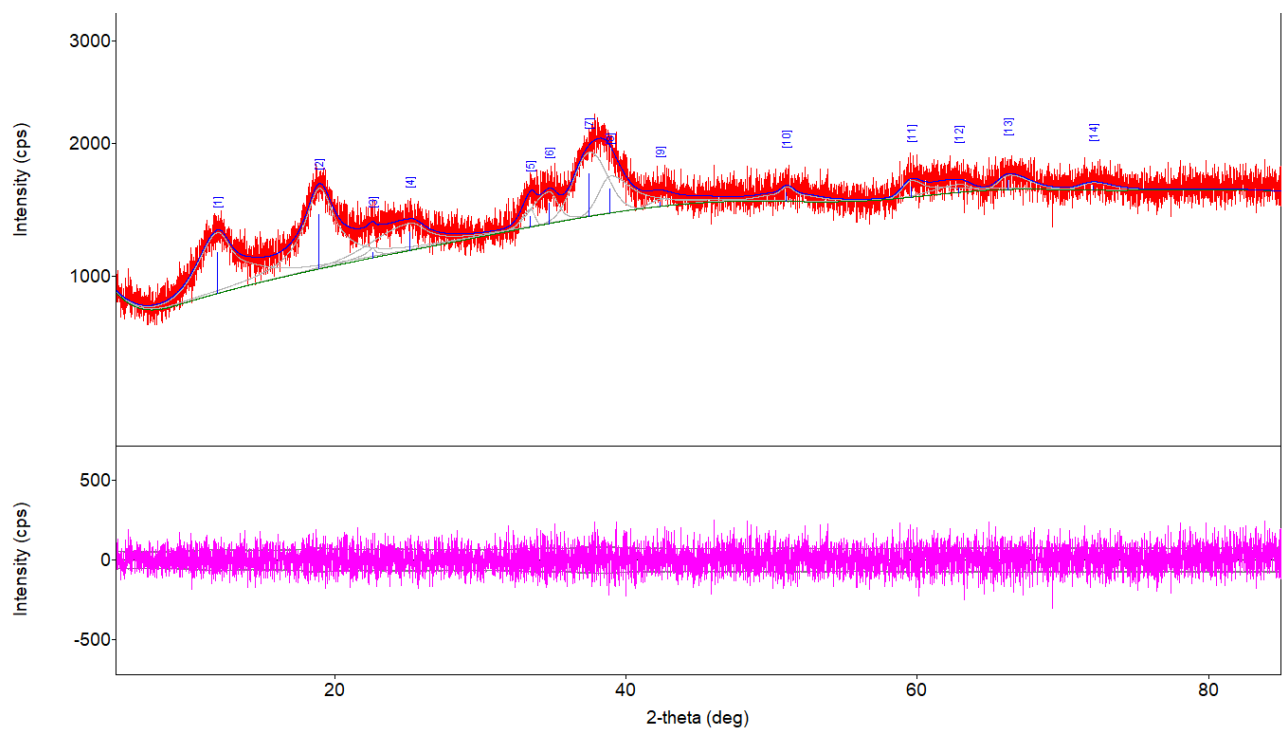


Figure S14. Fitting of the XRD pattern of the cobalt-doped Ni(OH)<sub>2</sub> anode exposed to 100 cycles of the ETAC process. Fitting was done by means of the PDXL2 (version 2.8.1.1) using pseudo-Voigt peak profile. In the top image: Red noisy curve is the measured signal; light blue is a manually fitted background curve; light green is fitting. The peaks are numbers 1 through 14 and ascribed in Table S3. In the bottom image: residual signal (fitted signal extracted from the measure one).

Table S3. Phase identification for the chemically aged cobalt-doped Ni(OH)<sub>2</sub> anode. Peak numbers (#) correspond to Figure S13. ICDD 00-038-0715, 00-014-0117, 00-059-0464 and 00-006-0075 were used as references for the  $\alpha$ -Ni(OH)<sub>2</sub>,  $\beta$ -Ni(OH)<sub>2</sub>,  $\beta$ -NiOOH and  $\gamma$ -NiOOH phases, respectively. d (Å) – d-spacing; FWHM (deg) – full width at half maximum; Int. I (cps deg) – peak intensity; Size (Å) – domain size.

#	2 $\theta$ (deg)	Expected 2 $\theta$ (deg) (from the relevant crystallographic database)	Phase/Plane	d (Å)	FWHM (deg)	Int. I (cps deg)	Size (Å)
1	12.0	12.82	(003) $\gamma$ -NiOOH	7.3990	2.9	1213	29
		11.349	(003) $\alpha$ -Ni(OH) <sub>2</sub>				
2	18.9	19.192	(002) $\beta$ -NiOOH	4.6856	2.4	1529	35
		19.258	(001) $\beta$ -Ni(OH) <sub>2</sub>				
3	22.6	22.735	(006) $\alpha$ -Ni(OH) <sub>2</sub>	3.9326	0.9	79	97
4	25.2	N/A	Amorphous halo of carbon	3.5341	4.4	722	19
5	33.4	33.458	(101) $\alpha$ -Ni(OH) <sub>2</sub>	2.6800	1.0	93	88
6	34.7	34.412	(012) $\alpha$ -Ni(OH) <sub>2</sub>	2.5841	2.0	369	43
7	37.5	37.93	(102) $\gamma$ -NiOOH	2.3986	2.6	963	33
		37.894	(201) $\beta$ -NiOOH				
8	38.9	N/A	?	2.3129	2.7	740	33
9	42.4	43.25	(105) $\gamma$ -NiOOH	2.1321	2.5	165	36
10	51.0	N/A	?	1.7889	1.7	287	53
11	59.6	59.981	(110) $\alpha$ -Ni(OH) <sub>2</sub>	1.5510	2.0	308	48
		60.240	(003) $\beta$ -Ni(OH) <sub>2</sub>				
		60.016	(006) $\beta$ -NiOOH				
12	62.9	N/A	?	1.4773	2.9	129	34
13	66.2	66.289	(311) $\beta$ -NiOOH	1.4097	2.4	214	41
		66.696	(-311) $\beta$ -NiOOH				
		66.23	(110) $\gamma$ -NiOOH				
14	72.1	N/A	?	1.3091	2.6	131	40

### S3.2 FIB sample preparation

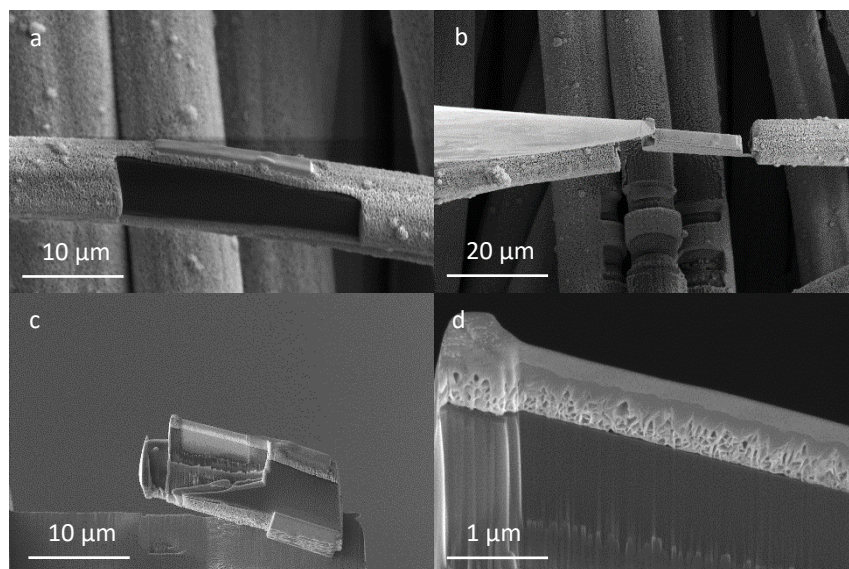


Figure S15: FIB sample preparation of a thin lamella of a nickel hydroxide layer for cross-section TEM analysis. The layer was deposited for 15 min at 15 mA/cm<sup>2</sup>.

### S3.3 Qualitative EDS analysis

Qualitative EDS analysis in several spots across the layer suggests a Ni: Co ratio of ca. 10:1, see Table S4.

Table S4: Qualitative EDS elemental analysis of the CC-supported cobalt-doped nickel hydroxide anode presented in Figure 3.

Element	Substrate (at. %)	Layer (at. %)
C (K)	98.3±3.8	34.5±0.5
O (K)	0	22.6±0.3
Co (K)	0	0.9±0.1
Ni (K)	0	8.5±0.3
Cu (K)	1.7±0.7	31.2±0.6
Pt (L)	0	2.3±0.3

### S3.4 HRSEM micrographs

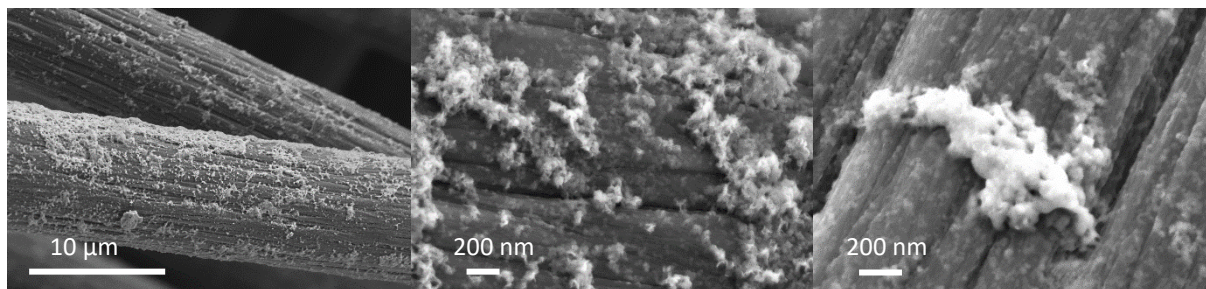


Figure S16: SEM micrographs of an anode prepared by deposition for 5 s at 30 mA/cm<sup>2</sup> (0.15 C/cm<sup>2</sup>).

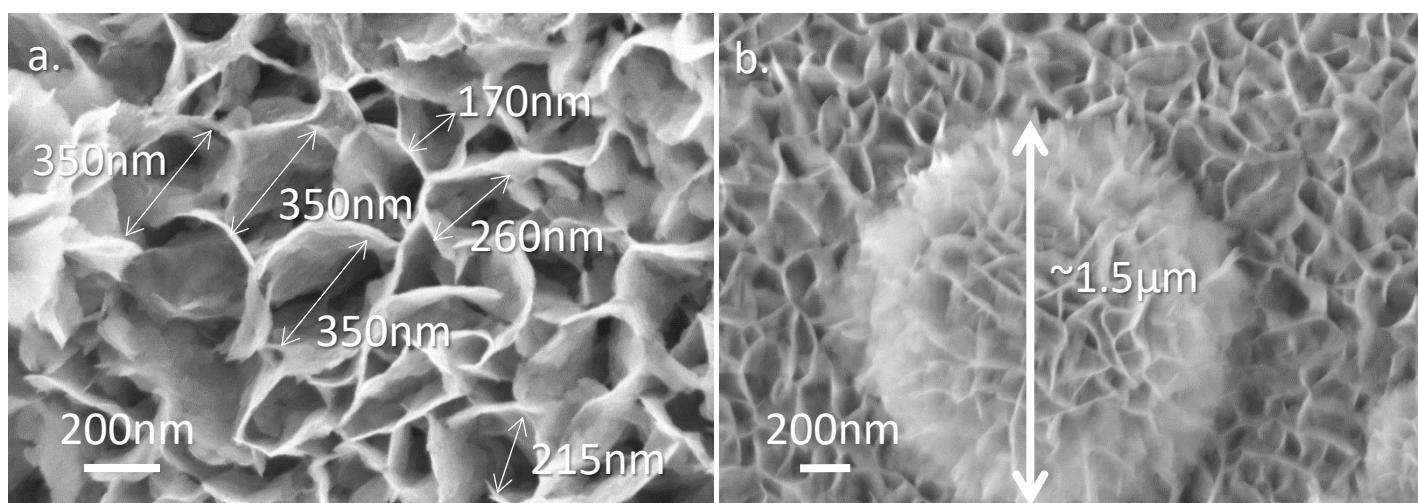


Figure S17: (a) HRSEM micrographs of the surface of the nickel hydroxide layer after 1 min deposition at 30 mA/cm<sup>2</sup> (1.8 C/cm<sup>2</sup>), (b) A nickel hydroxide sphere appearing after 2 min deposition at 30 mA/cm<sup>2</sup> (3.6 C/cm<sup>2</sup>).

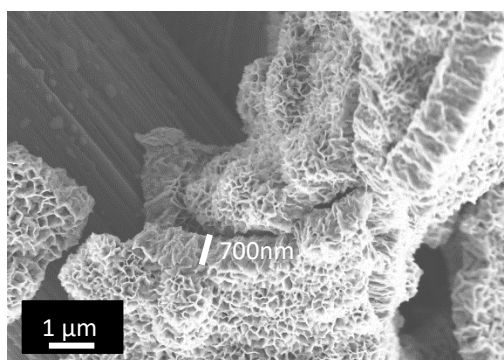


Figure S18: HRSEM micrograph of a peeled section of a nickel hydroxide layer deposited for 8 min at 30 mA/cm<sup>2</sup> (216 C/cm<sup>2</sup>).

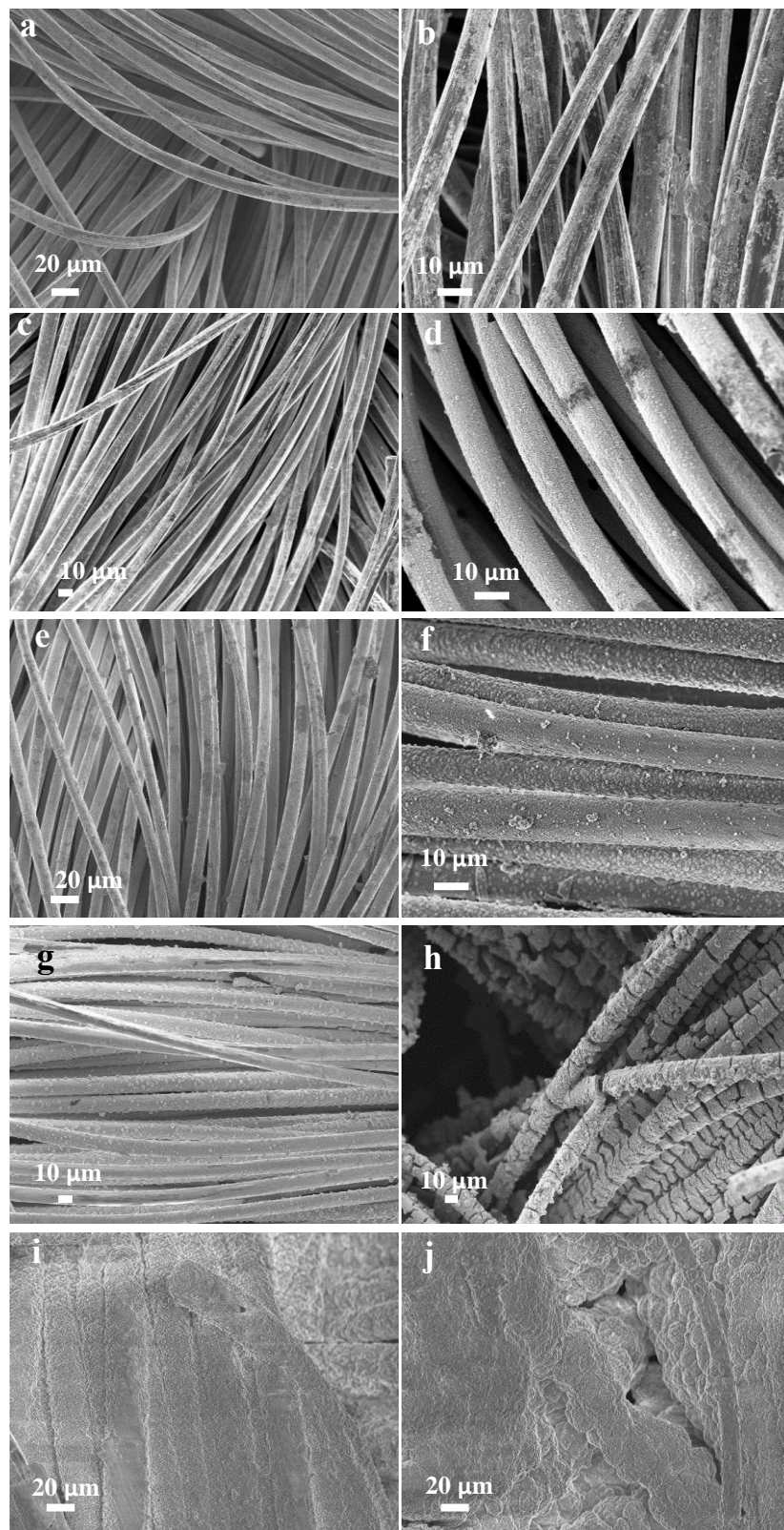
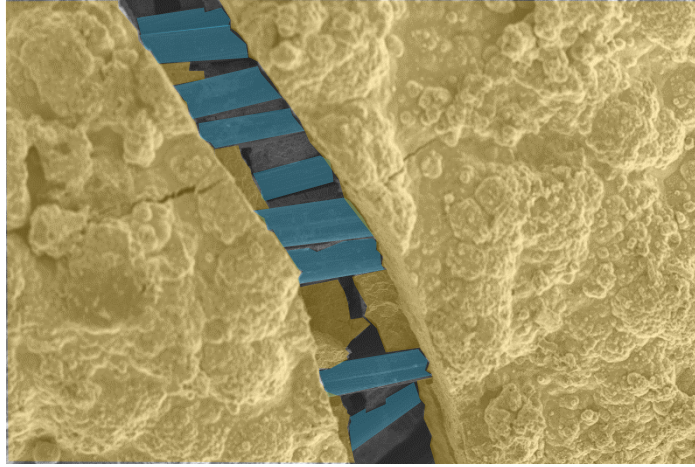


Figure S19: HRSEM micrographs of nickel hydroxide layers deposited at 30 mA/cm<sup>2</sup> for 5s (a), 10 s (b), 30 s (c), 1 min (d), 2 min (e), 4 min (f), 8 min (g), 30 min (h), 1 h (i) and 2h (j).



*Figure S20:* HRSEM micrographs of a nickel hydroxide layer deposited at 30 mA/cm<sup>2</sup> for 2 h.

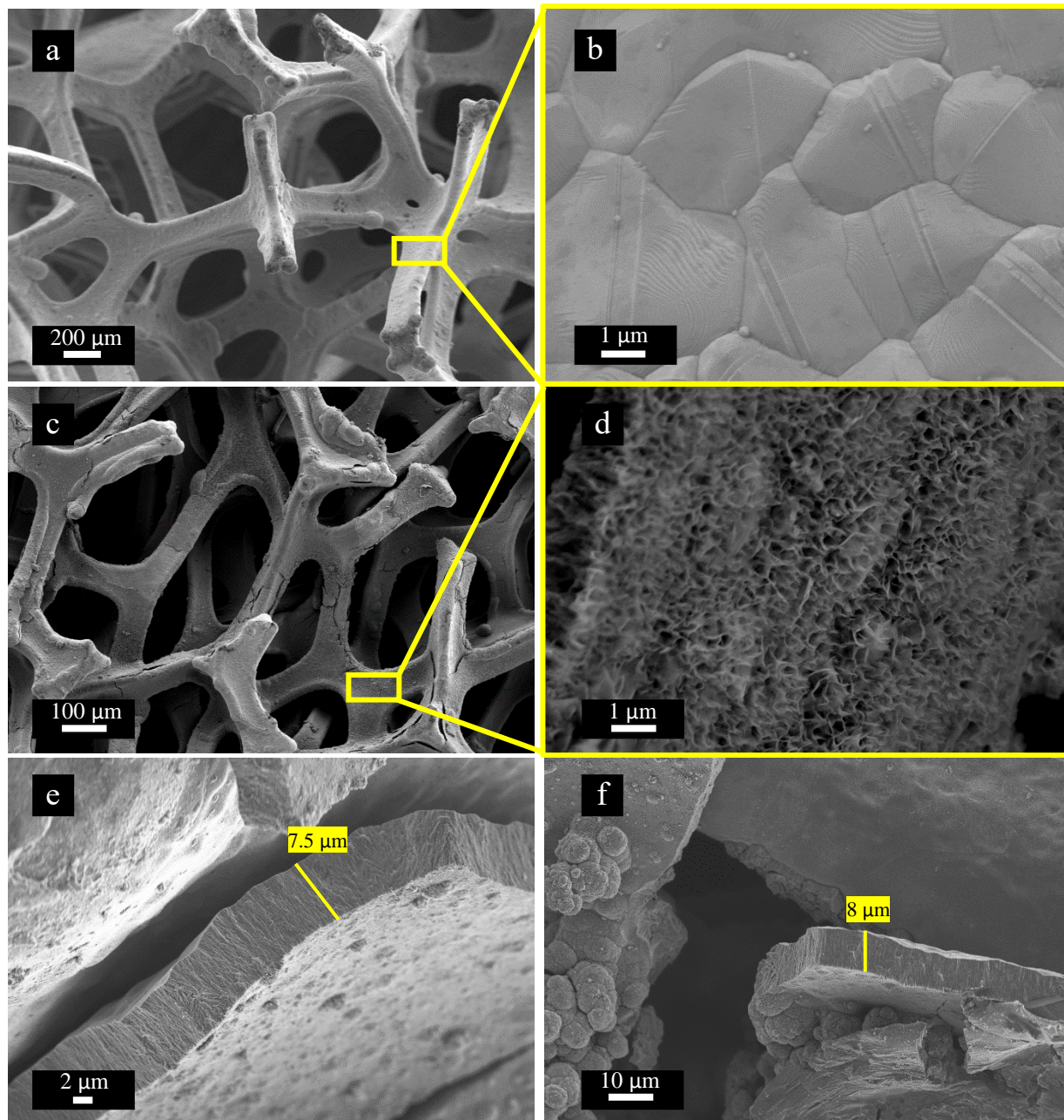


Figure S21: HRSEM micrographs of a bare nickel foam (a-b); and nickel hydroxide layer deposited onto this substrate at 30 mA/cm<sup>2</sup> for 2 h (c-f).

## **S4. Quantitative chemical composition analysis**

### **S4.1. Inductively coupled plasma atomic emission spectroscopy (ICP-AES)**

The averaged macroscopic chemical composition of the samples was analyzed by means of inductively coupled plasma atomic emission spectroscopy (ICP-AES) using ICAP 6300 Series Duo spectrometer (Thermo Scientific): radio frequency generator with the power of 1150 W, pump rate of 50 rpm, auxiliary gas flow rate of 0.5 L min<sup>-1</sup> and nebulizer gas flow rate of 0.7 L min<sup>-1</sup>. The samples for the ICP-AES tests were prepared to meet the following requirements: the concentration of the elements of interest (Ni and Co ions, in our case) within the range of 0.01-10 mg/L; no organic matter present; the overall salt concentration not exceeding 0.3 wt%. The electrodes (carbon cloth supported active mass mainly composed of Ni(OH)<sub>2</sub>) were cut into several pieces (with the overall mass not exceeding 30 mg). The dry pieces were weighed on an analytical balance with the accuracy of no less than 0.5 mg and placed in conical flasks (50 ml). To dissolve the electrode active mass, 4 ml of nitric acid HNO<sub>3</sub> (70%, BioLOab, AR) and 1.5 ml of hydrogen peroxide (30%, Merck, for analysis) were added to the flasks and heated up to 50 °C with the magnetic stirring. The use of the concentrated HNO<sub>3</sub> and H<sub>2</sub>O<sub>2</sub> ensured the removal of any possible organic impurity in the solutions. Intense O<sub>2</sub> evolution due to H<sub>2</sub>O<sub>2</sub> catalytic decomposition was observed and it was used as a visual indication of the ongoing dissolution process. Several aliquots of 1.5 ml H<sub>2</sub>O<sub>2</sub> were added in a sequence, until the full active mass dissolution was achieved (with no O<sub>2</sub> evolution). The solutions were transferred to volumetric flasks (50 ml) and diluted with the use of DDW. The remaining carbon cloth was washed, dried at 110 °C for 2.5 h in an oven in the air and weighed. Aliquots of 500 µl of those solutions were collected to be further diluted by 49.5 ml of DDW and to result in the final sample solutions for the ICP-AES measurements. The final dilution of 100 times was done to achieve the required <0.3 wt% of the salt concentration in the solution.

### **S4.2 Energy dispersive X-ray spectroscopy (EDS) and wavelength dispersive X-ray spectroscopy (WDS)**

The electron probe x-ray microanalysis was performed on a Quanta 200 (FEI, USA) scanning electron microscope equipped with an INCA (Oxford Instruments, England) energy dispersive spectrometer (EDS) and wavelength dispersive spectrometer (WDS). EDS measurements were carried out at the accelerating voltage of 20 kV, the probe current of about 0.5 nA at the working distance of 10 mm. The take-off angle of x-ray radiation was 35°. Acquisition time was 50 s per single measurement. For all cases, the standard deviation of the measured intensity for a single measurement did not exceed 5% relative. Quantitative

analysis was performed using the conventional ZAF correction procedure<sup>1</sup> included in the INCA software. Final results were normalized to 100 % for a sum of elements. WDS measurements were carried out using the accelerating voltage of 20 KV, the probe current of about 30 nA at the optimal working distance of 11 mm. The take-off angle of x-ray radiation was 30°. Acquisition time was 20 s per single measurement. Relative intensities of Co, Ni, and Fe K $\alpha$  analytical lines were measured with pure Co, Ni, and Fe standards respectively. The sample size was 4 points per specimen. Quantitative analysis was performed using the conventional ZAF correction procedure included in the INCA software<sup>1</sup>.

## **S5. Electrochemical characterizations**

Three CC-supported nickel hydroxide anodes were made at different combinations of current densities (5, 15, 30 and 60 mA/cm<sup>2</sup>) and charge densities (27, 54, 108 and 216 C/cm<sup>2</sup>). After initial charging at an anodic current density of 2.5 mA/cm<sup>2</sup> until reaching the OER plateau, the anode undergoes discharge at a cathodic current density of 2.5 mA/cm<sup>2</sup> until reaching a cut-off potential of 1V<sub>RHE</sub>. The total charge that was transferred during the discharge process was measured for each anode, and the average charge transferred during the discharge step for each set of deposition conditions is presented in Figure 7 in the article.

As expected, the charge that was transferred during the electrochemical discharge increases for anode that were deposited with higher charge densities, i.e., larger loading of the active material. Comparison between anodes that were deposited different current densities to the same charge density reveals improved electrochemical performance, in terms of the discharged charge, with higher deposition current density. The anodes deposited at current densities of 30 and 60 mA/cm<sup>2</sup> were selected for the E-TAC water splitting tests (highlighted in yellow).

The electrochemical charge utilization values after electrochemical discharge at 2.5 mA/cm<sup>2</sup> are presented in Figure S22. The electrochemical charge utilization is the ratio between the discharged charge and the theoretical charge calculated by multiplying the weight of deposited layer by the theoretical capacity of nickel hydroxide (1040C/g<sub>Ni(OH)<sub>2</sub></sub>).<sup>2</sup> For the anodes deposited at 60 mA/cm<sup>2</sup> for 7.5, 15, 30 and 60 minutes, the charge utilization decreases with increasing loading of the active layer.

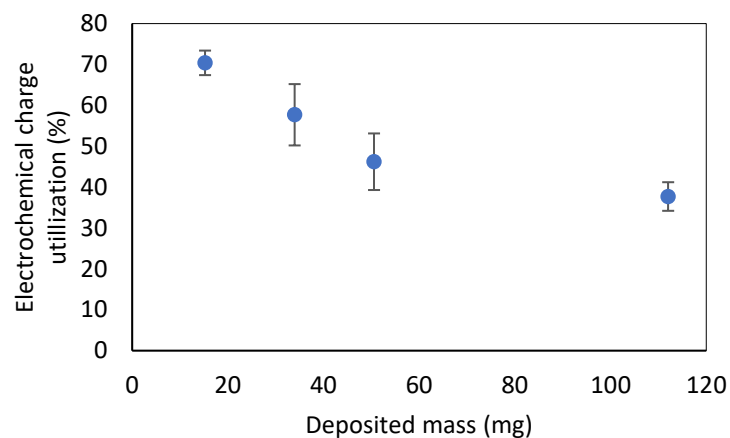


Figure S22: Electrochemical charge utilization values for anodes deposited at 60 mA/cm<sup>2</sup> for 7.5, 15, 30, 60 minutes (27, 54, 108 and 216 C/cm<sup>2</sup>).

A comparative performance assessment of all the anodes that were deposited at 30 and 60 mA/cm<sup>2</sup> was carried out by charging the anodes at current densities of 5, 10, 20 and 50 mA/cm<sup>2</sup> until cutoff potentials of 1.5, 1.52, 1.54, 1.56 and 1.58 V<sub>RHE</sub>, respectively. Then the anodes were discharged at a current density of 5 mA/cm<sup>2</sup> until a cutoff potential of 1 V<sub>RHE</sub>. This was repeated 15 times for each current density until stabilization. The charge capacities of the anodes are presented in Figure S23.

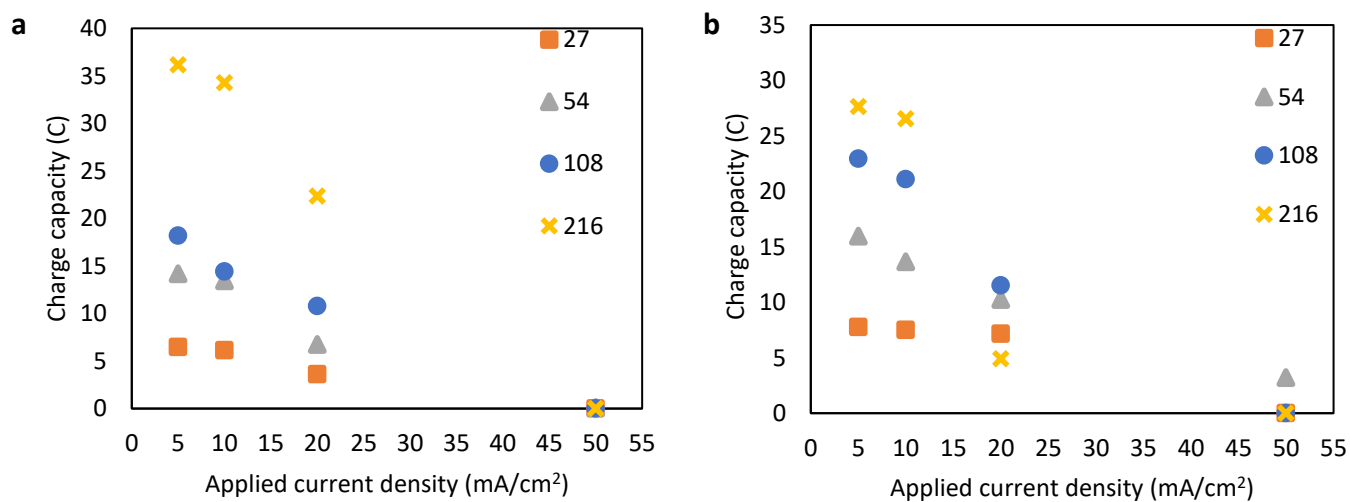


Figure S23: The charge capacities during galvanostatic charging at various current densities of (5, 10, 20 and 50 mA/cm<sup>2</sup>). For (a) anodes deposited at a current density of 30 mA/cm<sup>2</sup> for 15, 30, 60 and 120 min (corresponding to deposited charge densities of 27, 54, 108 and 216 C/cm<sup>2</sup>); and (b) anodes deposited at a current density of 60 mA/cm<sup>2</sup> for 7.5, 15, 30 and 60 min (corresponding to deposited charge densities of 27, 54, 108 and 216 C/cm<sup>2</sup>).

As shown in Figure S23 the anodes display appreciable charge capacity upon charging at current densities up to 20 mA/cm<sup>2</sup>. Upon charging at 50 mA/cm<sup>2</sup>, the potential of most of the anodes rose above the cutoff potential immediately after the measurement started, suggesting that the anode is not suitable for charging at such high current density. It should be noted that the characterization set up was preliminary, and all measurements were carried out with un-optimized electrical connections, which might have yielded anodes with significantly lower capacities than the ones achieved with an optimal set up.

## S6. E-TAC tests

Anodes for E-TAC water splitting tests were deposited at 30 or 60 mA/cm<sup>2</sup> for 15, 30, 60 and 120 min or 7.5, 15, 30 and 60 min, respectively. Three duplicates were prepared under each condition. The one with the best electrochemical charge-discharge performance was tested in 100s/100s E-TAC cycles at a charging current of 20 mA (10 mA/cm<sup>2</sup>) during the electrochemical stage. Two criteria were examined: the onset of parasitic oxygen evolution upon reaching the potential plateau (as discussed in the article, see Figure 10b), and the applied potential during charging up to this point.

Figures S24a and S24b present the charging potential during the charging stage of the 100s/100s E-TAC water splitting tests for the anodes that were deposited for different times at a current density of 60 and 30 mA/cm<sup>2</sup>, respectively. The results presented in these graphs are the average charging potentials of 5 repetitive 100s/100s E-TAC cycles for each of the anodes.

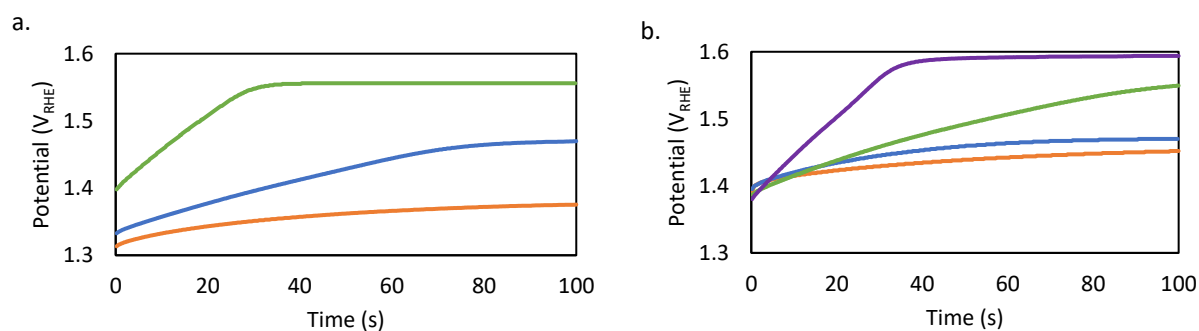


Figure S24: (a) The charging potential during galvanostatic charging at a constant current of 20 mA (10 mA/cm<sup>2</sup>) in 100s/100s E-TAC cycles for anodes deposited at a current density of 30 mA/cm<sup>2</sup> for 30, 60 and 120 min (corresponding to deposited charge densities of 54 (green), 108 (blue) and 216 C/cm<sup>2</sup> (orange)); and (b) for anodes deposited at a current density of 60 mA/cm<sup>2</sup> for 7.5, 15, 30 and 60 min (corresponding to deposited charge densities of 27 (purple), 54 (green), 108 (blue) and 216 C/cm<sup>2</sup> (orange)).

Figures S24a and S24b show that lower charging potentials were achieved for anodes that were deposited longer (i.e., to a larger charge density). Figure S21a shows no sign of reaching the OER potential plateau during 100 s charging (at 20 mA) for the anodes that were deposited at current density of 60 mA/cm<sup>2</sup> for 30 and 60 min (108 and 216 C/cm<sup>2</sup>). The anodes that were deposited at the same current density for shorter time (15 and 7.5 min, i.e., 54 and 27 C/cm<sup>2</sup>) displayed oxygen evolution with oxygen bubbles that started to appear at the anode after 90 s and 35 s, respectively.

Figure S24b shows that only the anode that was deposited for 2 h at current density of 30 mA/cm<sup>2</sup> (i.e. charge density of 216 C/cm<sup>2</sup>) succeeded charging for 100 s without notable amounts of oxygen evolution. For the anodes that were deposited at the same current density for shorter time (1 h and 30 min, i.e., 108 and 54 C/cm<sup>2</sup>) displayed oxygen evolution with oxygen bubbles that started to appear at the working anode after 70 and 30 s, respectively. The anode that were deposited under current density of 30 mA/cm<sup>2</sup> for 15 min (i.e., charge density of 27 C/cm<sup>2</sup>) was not examined since the anodes that were deposited at the same current density but in a larger charge densities already failed at the 100s/100s E-TAC test and reached to the OER plateau region.

Only the anodes that did not produce oxygen during the 100s/100s E-TAC test went through additional 200s/200s and 400s/400s E-TAC cycles. the average charging potentials of 3 repetitive E-TAC cycles for each of these anodes are presented in Figure S25.

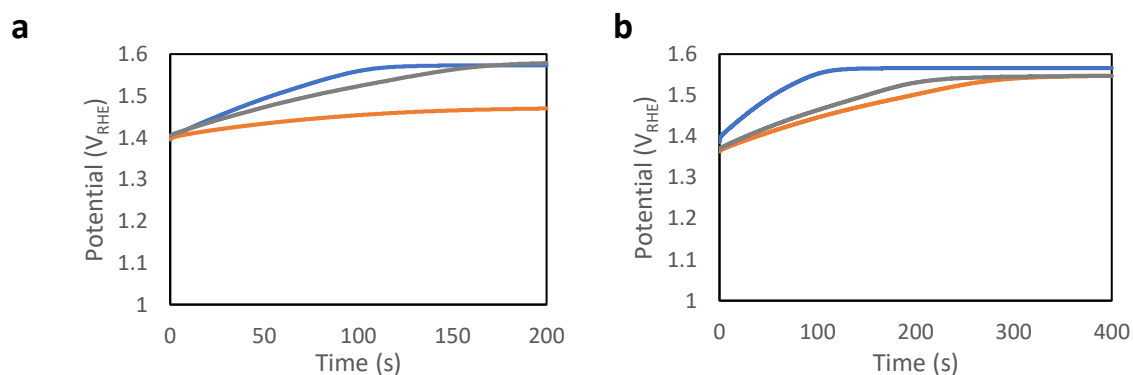


Figure S25: The charging potential during galvanostatic charging at a constant current of 20 mA (10 mA/cm<sup>2</sup>) in (a) 200s/200s and (b) 400s/400s E-TAC cycles, for anodes deposited at a current density of 30 mA/cm<sup>2</sup> for 120 min (216 C/cm<sup>2</sup>, grey), 60 mA/cm<sup>2</sup> for 30 min (108 C/cm<sup>2</sup>, blue) and 60 mA/cm<sup>2</sup> for 60 min (216 C/cm<sup>2</sup>, orange).

Figure S25a shows the charging potentials of the selected anodes during 200s/200s E-TAC cycles. OER plateau is reached after 130 s for the anode that were deposited at current density of 60 mA/cm<sup>2</sup> for 30

min ( $108 \text{ C/cm}^2$ ). Figure S25b shows the charging potentials of the selected anodes during 400s/400s E-TAC cycles. OER plateau is reached for the anode that were deposited at current density of  $30 \text{ mA/cm}^2$  for 2 h ( $216 \text{ mA/cm}^2$ ) after 220s and for the anode that were deposited at current density of  $60 \text{ mA/cm}^2$  for 1h ( $216 \text{ mA/cm}^2$ ) after 270 s.

Figure S26 presents a summary of the E-TAC tests results. The bars at the graph represents the average potential during the charging step and the margins of the bars represents the starting and the ending potentials during the charging step.

We note that the average potential was calculated at the optimal working window for each anode, from the beginning of the charging step until the OER plateau potential. The inset compares between the maximum charge that each anode could reach during E-TAC cycles without reaching the OER plateau region. The charge was calculated by duplicating the current density used at the charging stage ( $10 \text{ mA/cm}^2$ ) by the duration of the charging until reaction the OER plateau.

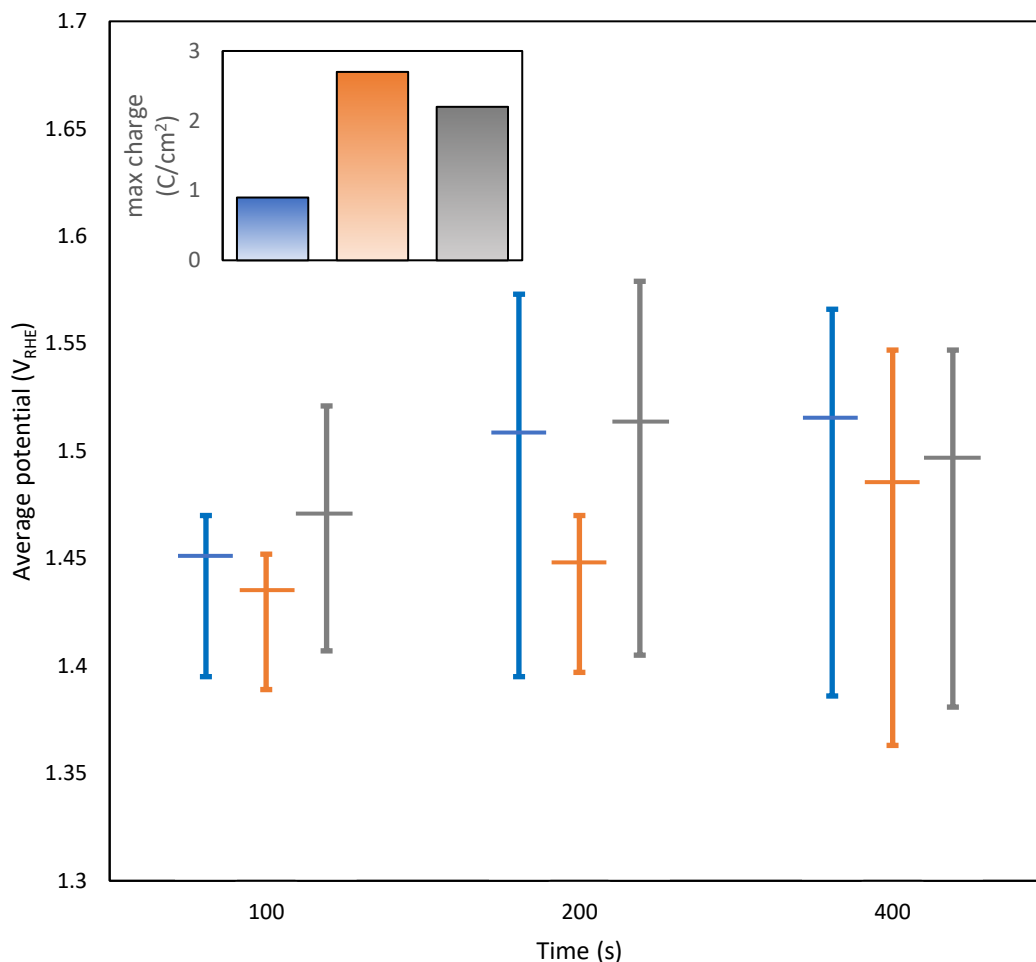


Figure S26: E-TAC water splitting tests. Charging potential range during galvanostatic charging at a constant current of 20 mA (corresponding to an aerial current density of 10 mA/cm<sup>2</sup>) vertical lines, (|) and average horizontal lines, (—) during the oxygen-free charging stage in 100 s/100 s, 200 s, 200 s and 400 s / 400 s E-TAC cycles. Upper graph charge densities that could be charged until the OER plateau during all E-TAC tests. In gray- anode deposited at a current density of 30 mA/cm<sup>2</sup> for 120 min (216 C/cm<sup>2</sup>), in blue- anode deposited at 60 mA/cm<sup>2</sup> for 30 min (108 C/cm<sup>2</sup>) and in orange- anode deposited at 60 mA/cm<sup>2</sup> for 60 min (216 C/cm<sup>2</sup>)

As shown in Figure S26, the highest regenerated charge capacities (i.e., the charge capacity that can be extracted by the chemical regeneration reaction, rxn. 3) was obtained for the anode deposited at 60 mA/cm<sup>2</sup> for 1 h (216 C/cm<sup>2</sup>). Therefore, this electrode was further characterized and compared to its counterpart NF-supported anode. Two duplicates of this anode that were deposited under the same conditions were examined for the E-TAC test results presented in Figure 9 in the article.

Figure S27 presents different magnification HRSEM images of sample that has undergone through 100 E-TAC cycles.

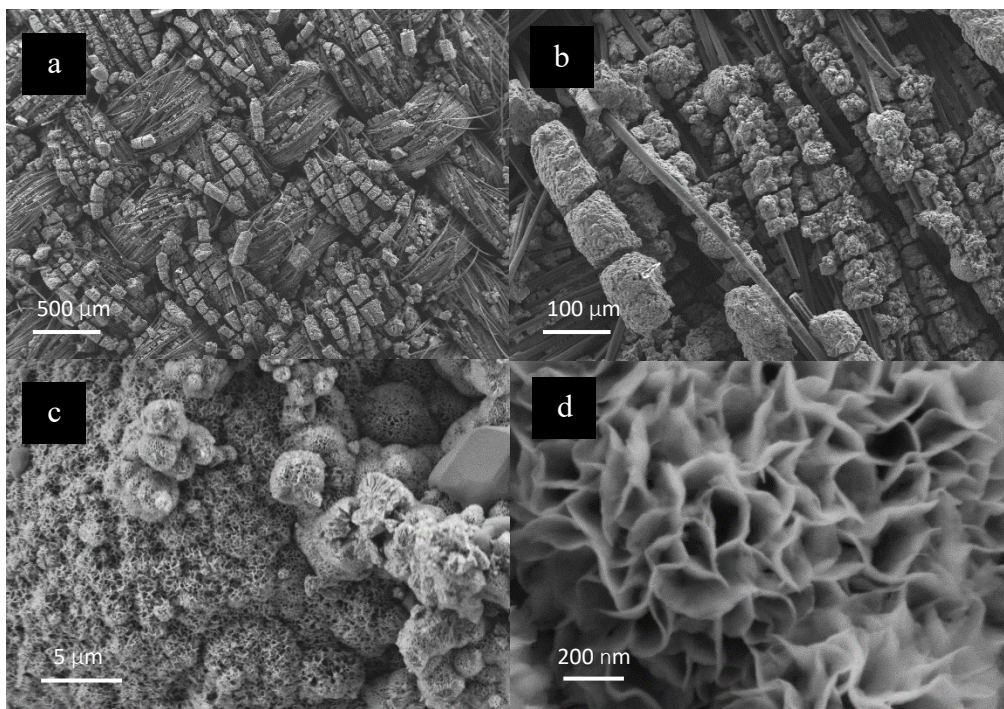


Figure S27: HRSEM micrographs of nickel hydroxide anodes deposited on hydrophilic carbon cloth substrates at a current density of 60 mA/cm<sup>2</sup> for 1h after 100 E-TAC cycles at different magnifications (a) 100x, (b) 500x, (c) 10Kx and (d) 170 Kx.

## S7. Dissolved oxygen measurements

Figure S28 presents a digital image of the dissolved oxygen (DO) measurement setup. The setup consisted of a sealed 5-neck flask with insertions for the working, counter and reference electrodes, and for the DO probe. The 5<sup>th</sup> insertion is for flushing with nitrogen gas (99.999%, Maxima). The DO probe (VisiFerm RS-485, Hamilton) was placed horizontally to minimize bubble buildup on its surface. All the DO measurements were carried in 5M KOH aqueous electrolyte, at ambient temperature, under vigorous magnetic stirring.

To calibrate the response of the DO probe, a Pt foil was first connected as a working electrode, with a charged Ni(OH)<sub>2</sub> counter electrode and an Hg/HgO reference electrode (RE-6, ALS Co., 0.118 V<sub>SHE</sub>), and a constant current was applied for varying times, similar to the tests described in Section 2.5 in the article. Considering that the only reaction taking place at a Pt electrode under anodic polarization in 5M KOH electrolyte is the oxygen evolution reaction (OER),<sup>2</sup> the amount of oxygen produced by the Pt electrode during the anodic polarization can be calculated by Faraday's law of electrolysis. The DO probe's response

was then plotted versus the calculated oxygen amount to construct the calibration curve presented in Figure S29. This calibration curve was then used in consequent tests to calculate the Faradaic efficiency for the nickel hydroxide anode charging reaction, as described in the article.

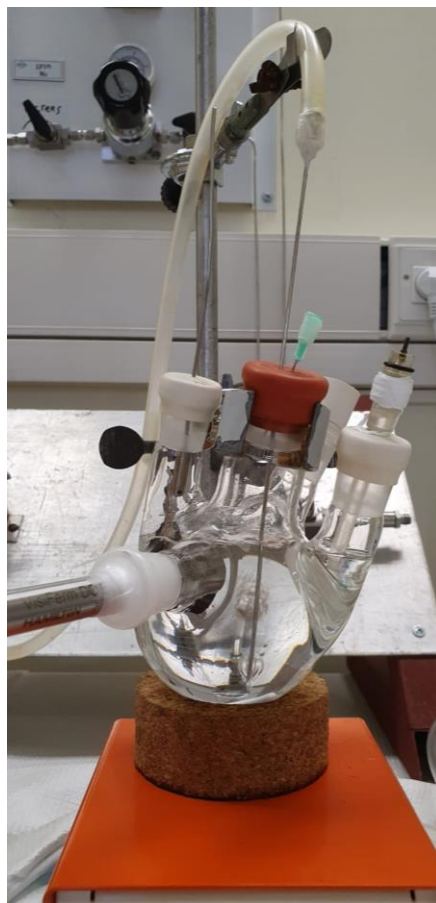


Figure S28: Photograph of the DO measurement setup.

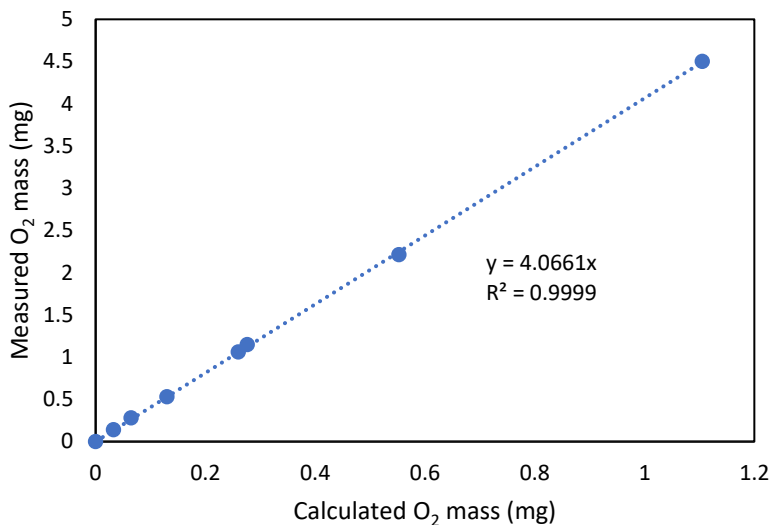


Figure S29: Calibration curve for the DO probe. The x-axis values present the amount of O<sub>2</sub> generated at the Pt electrode, calculated by Faraday's law of electrolysis. The y-axis values present the amount of O<sub>2</sub> measured by the DO probe.

To evaluate the beginning of the OER plateau, a differential of the potential response with time ( $dE/dt$ ) was calculated for each test, and the plateau was estimated at a point in time wherein a distinct change in the derivative was observed (see Figures 12b and 12c in the article). To evaluate the corresponding DO signal onset, a derivative of the DO response with time ( $dDO/dt$ ) was calculated, and the onset time was taken at the point in time wherein the derivative rose above  $\sim 0$ . This value was then compared to the DO onset point from the direct response of the DO with time ( $DO(t)$ ), to reduce error.

## References:

1. S. J. B. Reed, *Electron Microprobe Analysis*, Cambridge University Press, Cambridge, (1975).
2. Symes, M. D. & Cronin, L. Decoupling hydrogen and oxygen evolution during electrolytic water splitting using an electron-coupled-proton buffer. *Nat. Chem.* **5**, 403 (2013).
3. Oliva, P. et al. Review of the structure and the electrochemistry of nickel hydroxides and oxyhydroxides. *J. Power Sources* **8**, 229–255 (1982).